Symmetry breaking and phase transitions in Bose-Einstein condensates with spin–orbital-angular-momentum coupling

Y. Duan[1,2] Y. M. Bidasyuk[1] and A. Surzhykov[1,2,3]

[1]*Physikalisch–Technische Bundesanstalt, D–38116 Braunschweig, Germany*
[2]*Institut für Mathematische Physik, Technische Universität Braunschweig, D–38106 Braunschweig, Germany*
[3]*Laboratory for Emerging Nanometrology Braunschweig, D–38106 Braunschweig, Germany*

Theoretical study is presented for a spinor Bose-Einstein condensate, whose two components are coupled by copropagating Raman beams with different orbital angular momenta. The investigation is focused on the behavior of the ground state of this condensate, depending on the atom-light coupling strength. By analyzing the ground state, we have identified a number of quantum phases, which reflect the symmetries of the effective Hamiltonian and are characterized by the specific structure of the wave function. In addition to the well-known stripe, polarized, and zero-momentum phases, our results show that the system can support phases whose wave functions contain a complex vortex molecule. Such a molecule plays an important role in the continuous phase transitions of the system. The predicted behavior of vortex-molecule phases can be examined in cold-atom experiments using currently existing techniques.

I. INTRODUCTION

The first experimental realizations of atomic Bose-Einstein condensates (BECs) in 1995 opened a new era in the study of macroscopic quantum systems [1,2]. In the original experiments, the condensation of atoms in a single hyperfine sublevel was achieved using a magnetic trap. Further developments of optical-dipole trapping techniques enabled the simultaneous confinement of atoms in several hyperfine substates and thus opened a possibility to also manipulate the spin degree of freedom of the condensate [3,4]. Coherent coupling between the substates of such spinor condensate is commonly achieved with two-photon Λ-type Raman transitions. If the Raman transition is accompanied by a change in the center-of-mass motion of an atom, the spin and motional degrees of freedom become coupled. This artificial spin-orbit coupling (SOC) has drawn considerable attention from both theory and experiment [5–10]. In particular, previous studies demonstrated the utility of atomic BECs as a highly controllable platform for exploring effects of SOC in various fields of modern physics [10]. As the most prominent example, a spin-orbit-coupled condensate has been proposed to simulate such exotic phenomena in condensed-matter physics as topological insulators and quantum spin Hall effect [11,12]. Moreover, BEC with SOC can be seen as a test bed for studying quantum phase transitions at zero temperature, as it supports a number of quantum phases with distinct symmetries and topological properties [13–17].

So far, different experimental setups have been proposed to produce spin-orbit-coupled condensates [10]. In the first realization, for example, counterpropagating Raman lasers were used to enable a transfer of linear momentum to atoms during the "absorption-and-stimulated-emission" process [5]. In ad-

dition to this spin-linear-momentum (SLM) coupling, another type of SOC can be induced by two copropagating beams with different orbital angular momenta [18]. This setup suppresses the transfer of linear momentum and couples instead the spin and orbital angular momentum (OAM) of the condensate. BECs with the spin–orbital-angular-momentum (SOAM) coupling have been studied theoretically [18–25] and realized recently in experiments with ⁸⁷Rb atoms [26,27]. In these studies, special attention has been paid to their rich ground-state phase diagram. In particular, it has been shown that several quantum phases in SOAM-coupled condensates are very similar to those observed under SLM coupling [21,27]. However, a few other phases, which have no obvious counterparts in the SLM scenario, were also predicted [22–25]. These phases are characterized by the existence of quantum vortices or other topological defects. A number of theoretical studies have been performed to search for such vortex phases and to analyze the complex topological structure of their wave functions [22–25]. Not so much attention, however, has been paid to the questions of how the vortex states change through the phase transitions and how these changes are related to the *symmetries* of the system. As we show below, answers to these questions are especially important for understanding the microscopic mechanism driving the phase transitions in SOAM-coupled atomic condensates.

In the present paper, we aim to analyze tight interrelations between the quantum phase transitions and symmetries in spinor BECs with SOAM coupling. To this end, we first define in Sec. II our model system. We consider a quasi-two-dimensional condensate whose two internal levels are resonantly coupled by copropagating Laguerre-Gaussian (LG) laser modes. The Gross-Pitaevskii Hamiltonian of this system as well as the properties of its eigenstates are discussed
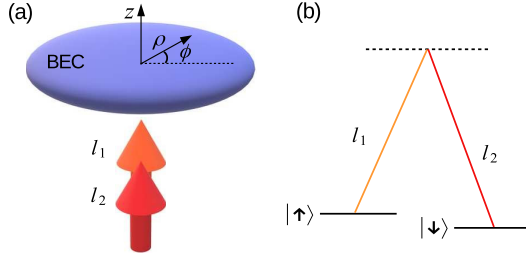
FIG. 1. (a) Schematic representation of a disk-shaped BEC interacting with copropagating LG laser beams with OAM l_1 and l_2. (b) A sketch of the level diagram illustrating the angular momentum transfer in the two-photon Raman transition between atomic states $|\uparrow\rangle$ and $|\downarrow\rangle$.

in Secs. II A and II B. The numerical procedure used to reliably compute the ground-state solutions of the Hamiltonian is briefly explained in Sec. II C. This procedure is employed later in Sec. III for a realistic scenario of ^{87}Rb condensate in a disk-shaped harmonic trapping potential. In particular, the ground-state wave function is calculated for various values of the Raman coupling strength. Based on the results of these calculations, we identify in total five quantum phases of the spinor condensate. We describe these phases and analyze the relation between their vortex structures and symmetry properties. Moreover, we argue that the quantum vortices in the condensate can strongly affect the mechanism of phase transitions. Particularly, we find that the counterintuitive continuous phase transitions, predicted for the SOAM coupled condensate, can be explained by the formation of a vortex molecule in the ground-state wave function. The summary and outlook are given in Sec. IV.

II. THEORETICAL FRAMEWORK

A. Model

We consider a weakly interacting BEC in a harmonic trap. The condensate atoms are assumed to occupy two internal atomic states, coupled by laser beams in a Λ-type Raman regime [see Fig. 1(b)]. For simplicity, we denote these two states as $|\uparrow\rangle$ and $|\downarrow\rangle$. The condensate is then described by a coherent superposition of two macroscopic wave functions as

$$\Psi(\mathbf{r}) = \psi_\uparrow(\mathbf{r})\chi_\uparrow + \psi_\downarrow(\mathbf{r})\chi_\downarrow. \tag{1}$$

For convenience of representation, we consider $\chi_\uparrow = \begin{pmatrix} 1 \\ 0 \end{pmatrix}$ and $\chi_\downarrow = \begin{pmatrix} 0 \\ 1 \end{pmatrix}$ as the basis of a two-dimensional complex Hilbert space. In such representation, $\Psi(\mathbf{r})$ can be written as a two-component vector

$$\Psi(\mathbf{r}) = \begin{bmatrix} \psi_\uparrow(\mathbf{r}) \\ \psi_\downarrow(\mathbf{r}) \end{bmatrix}. \tag{2}$$

This pseudo-spin-$\frac{1}{2}$ wave function Ψ obeys the Gross-Pitaevskii equation (GPE),

$$i\hbar\frac{\partial}{\partial t}\Psi = \hat{H}\Psi \equiv (\hat{H}_s + \hat{H}_{int})\Psi, \tag{3}$$

where the Hamiltonian $\hat{H}$ is a 2×2 matrix consisting of single-particle and nonlinear interaction terms [23].

The first one,

$$\hat{H}_s = -\frac{\hbar^2\nabla^2}{2M}\mathbb{I}_2 + V_{trap}\mathbb{I}_2 + \hat{V}_c, \tag{4}$$

is a sum of kinetic energy operator, trapping potential and the Raman coupling $\hat{V}_c$ between two internal states. The interaction Hamiltonian $\hat{H}_{int}$ in Eq. (3) reads

$$\hat{H}_{int} = \begin{pmatrix} g_{\uparrow\uparrow}|\psi_\uparrow|^2 + g_{\uparrow\downarrow}|\psi_\downarrow|^2 & 0 \\ 0 & g_{\downarrow\downarrow}|\psi_\downarrow|^2 + g_{\uparrow\downarrow}|\psi_\uparrow|^2 \end{pmatrix}, \tag{5}$$

where $g_{\uparrow\uparrow}$, $g_{\downarrow\downarrow}$ and $g_{\uparrow\downarrow}$ are nonlinear interaction parameters characterizing collisions between particles in corresponding internal states.

To further specify the single-particle Hamiltonian (4), we need to define the geometry of our system. In particular, we consider the condensate to be confined in a disk-shaped harmonic trap as illustrated in Fig. 1(a). In cylindrical coordinates $\mathbf{r} = (\rho, \phi, z)$, the trap potential is described by

$$V_{trap}(\mathbf{r}) = \frac{M\omega_\rho^2\rho^2}{2} + \frac{M\omega_z^2 z^2}{2}, \tag{6}$$

where ω_z and ω_ρ are the trapping frequencies in z and radial directions, respectively. We assume $\omega_z \gg \omega_\rho$, which allows us to consider the z dimension as frozen and treat the system as two-dimensional [27,28].

As schematically shown in Fig. 1, a resonant Raman coupling between two atomic states is induced by two LG lasers with different OAM l_1 and l_2, which copropagate along the z axis. The coupling term $\hat{V}_c$ in Eq. (4) is then defined by the effective two-photon Rabi frequency [21]. In the paraxial regime, it reads as

$$\hat{V}_c(\mathbf{r}) = \tilde{\Omega}(\rho)\begin{pmatrix} 0 & e^{2il\phi} \\ e^{-2il\phi} & 0 \end{pmatrix} \equiv \tilde{\Omega}(\rho)\hat{\sigma}_{2l}, \tag{7}$$

where $2l = l_2 - l_1$ and the unitary operator $\hat{\sigma}_{2l}$ can be represented in terms of the Pauli matrices $\hat{\sigma}_x$ and $\hat{\sigma}_z$:

$$\hat{\sigma}_{2l} = e^{il\phi\hat{\sigma}_z}\hat{\sigma}_x e^{-il\phi\hat{\sigma}_z}. \tag{8}$$

Moreover, in Eq. (7), $\tilde{\Omega}(\rho)$ is the radial function, which reflects the intensity distribution of the LG modes and is given by

$$\tilde{\Omega}(\rho) = \Omega\left(\frac{\rho}{w}\right)^{2l} e^{-\frac{2\rho^2}{w^2}}, \tag{9}$$

where w is the beam waist and Ω is the amplitude parameter proportional to the beam intensity, which we call the *Raman coupling strength*.

To complete the introduction of the theoretical model, we should mention two integrals of motion of the GPE (3). These are the total particle number N, which we choose for the normalization of the wave functions

$$N = \int d\mathbf{r}(|\psi_\uparrow|^2 + |\psi_\downarrow|^2), \tag{10}$$

and the energy per particle

$$\epsilon = \frac{1}{N}\int d\mathbf{r}\Big[(\psi_\uparrow^*, \psi_\downarrow^*)\hat{H}_s(\psi_\uparrow, \psi_\downarrow)^T \\ + \frac{g_{\uparrow\uparrow}}{2}|\psi_\uparrow|^4 + \frac{g_{\downarrow\downarrow}}{2}|\psi_\downarrow|^4 + g_{\uparrow\downarrow}|\psi_\uparrow|^2|\psi_\downarrow|^2\Big]. \tag{11}$$

The latter expression allows us to define the ground state of the system as a state corresponding to the lowest possible value of ϵ.

B. Symmetry properties of the system

It is convenient to begin the analysis of the GPE (3) by addressing the noninteracting case $\hat{H}_{\text{int}} = 0$. The GPE in this case becomes a single-particle Schrödinger equation. To characterize its solutions, we need to analyze relevant symmetries defined by transformation operators commuting with the Hamiltonian $\hat{H}_s$. For a system with SOAM coupling, the relevant symmetry transformations include rotations and time reversal. It should be noted, however, that the time-reversal symmetry is specific to the case of resonant Raman coupling considered here.

We first analyze the rotational symmetry with respect to the z axis. Due to the ϕ dependence of Raman coupling $\hat{V}_c$, the single-particle Hamiltonian (4) is not invariant under rotation of spatial coordinates, which is generated by the operator

$$\hat{R}(\phi_0) = e^{-i\hat{L}_z\phi_0}, \quad \text{with} \quad \hat{L}_z = -i\frac{\partial}{\partial\phi}\mathbb{I}_2. \quad (12)$$

This means, in particular, that OAM projection $\langle\hat{L}_z\rangle = \frac{1}{N}\langle\Psi|\hat{L}_z|\Psi\rangle$ is not conserved in the system. On the other hand, the operator that combines spatial and spin rotation,

$$\hat{R}'(\phi_0) = e^{-i(\hat{L}_z - l\hat{\sigma}_z)\phi_0}, \quad (13)$$

commutes with the Hamiltonian (4) and therefore represents a symmetry of the system. This symmetry transformation implements the spatial rotation by the angle ϕ_0 with a simultaneous spin rotation by the angle $-l\phi_0$. We therefore expect the conservation of the total angular momentum (TAM) projection defined by the operator

$$\hat{J}_z = \hat{L}_z - l\hat{\sigma}_z. \quad (14)$$

One may note a conceptual similarity of our system to a standard SOC in atomic and nuclear physics. In contrast to atoms and nuclei, however, the eigenvalues of $\hat{J}_z$ for SOAM-coupled condensates span the entire range of integer values $-\infty < j < \infty$.

The eigenstates of the Hamiltonian (4) with well-defined TAM projection can be written in the general form

$$\Psi_j(\mathbf{r}) = \begin{bmatrix} f_j(\rho)e^{i(j+l)\phi} \\ g_j(\rho)e^{i(j-l)\phi} \end{bmatrix}, \quad (15)$$

where j is an eigenvalue of $\hat{J}_z$ operator and the radial functions $f_j(\rho)$ and $g_j(\rho)$ can be considered real-valued without a loss of generality [22]. In the discussion below, we will refer to the symmetry associated with the operator (13) as *rotational symmetry* (R symmetry) and to the states (15) as *rotationally-symmetric* states of the system. To identify these states, we can evaluate the symmetry indicators, given by the expectation value

$$\langle\hat{J}_z\rangle = \frac{1}{N}\langle\Psi|\hat{J}_z|\Psi\rangle \quad (16)$$

and a standard deviation

$$\Delta J_z \equiv \sqrt{\langle\hat{J}_z^2\rangle - \langle\hat{J}_z\rangle^2}. \quad (17)$$

By inserting $\Psi = \Psi_j$ into above equations, we obtain $\langle\hat{J}_z\rangle = j$ and $\Delta J = 0$. For a general non-R-symmetric state, we can expect $\Delta J > 0$. This measure will be used as a quantitative indicator of the rotational symmetry in our numerical calculations below.

As already mentioned above, another relevant symmetry transformation is the time reversal. The Hamiltonian $\hat{H}_s$ obviously commutes with the time-reversal operator $\hat{T} = \hat{\sigma}_x\hat{K}$, with $\hat{K}$ being the complex conjugation. Eigenfunctions of this operator, which correspond to real eigenvalues ± 1, have the following structure:

$$\Phi_\pm(\mathbf{r}) = \begin{bmatrix} \psi(\mathbf{r}) \\ \pm\psi^*(\mathbf{r}) \end{bmatrix}. \quad (18)$$

Here $\psi(\mathbf{r})$ is an arbitrary function which has no immediate relation to the functions $f(\rho)$ and $g(\rho)$ in Eq. (15). We will refer to the states (18) as *time-reversal-symmetric*. Again, we would like to have a convenient measure which quantifies the time-reversal symmetry of an arbitrary wave function (2). In contrast to the rotational symmetry, however, there is no physical observable associated with the operator $\hat{T}$. One suitable quantity, commonly applied for spinor condensates and related to T symmetry, is the spin polarization

$$\langle\hat{\sigma}_z\rangle = \frac{1}{N}\int(|\psi_\uparrow(\mathbf{r})|^2 - |\psi_\downarrow(\mathbf{r})|^2)d\mathbf{r}, \quad (19)$$

which represents the relative population imbalance between two components of the wave function [23,27]. This quantity, however, is not a universal indicator of the time-reversal symmetry. As one can see from Eq. (18), time-reversal-symmetric states are always unpolarized, $\langle\hat{\sigma}_z\rangle = 0$. The opposite, however, is not true, since the unpolarized state can be also non-T-symmetric. We will encounter such nonsymmetric unpolarized states in the numerical results of the next section.

Above we have analyzed each of the two symmetries of the system separately. We now discuss the consequences of both of them being applied simultaneously. We first remind the reader that the angular momentum operator transforms under time reversal as $\hat{T}\hat{J}_z\hat{T}^{-1} = -\hat{J}_z$. Consequently, for every eigenstate Ψ_j there is a corresponding eigenstate with opposite TAM projection Ψ_{-j} related by the following transformation

$$\hat{T}\Psi_j(\mathbf{r}) = \pm\Psi_{-j}(\mathbf{r}). \quad (20)$$

In general, this relation may contain an arbitrary phase factor which is restricted to only plus or minus if we consider radial functions in Eq. (15) to be real. The time-reversal symmetry of the Hamiltonian also implies that both $\Psi_j(\mathbf{r})$ and $\hat{T}\Psi_j(\mathbf{r})$ are eigenstates with the same energy. Since the states $\Psi_j(\mathbf{r})$ and $\Psi_{-j}(\mathbf{r})$ are orthogonal for $j \neq 0$, then corresponding energy levels are doubly degenerate. The state with $j = 0$ is nondegenerate and possesses both symmetries. This additionally restricts the radial parts of the corresponding wave function to $g_0(\rho) = \pm f_0(\rho)$.

The above considerations are valid for all eigenstates of the Hamiltonian $\hat{H}_s$. However, our primary goal here is to characterize the properties of the ground state. According to the previous studies [20,22,23], the ground state of a SOAM-coupled system may have either zero or nonzero angular momentum projection j_0 within the range $-l \leqslant j_0 \leqslant l$. If the

ground state corresponds to zero angular momentum $j_0 = 0$, then it is also T symmetric as already discussed above. For the cases when $j_0 \neq 0$, there are two degenerate rotationally symmetric ground states Ψ_{j_0} and Ψ_{-j_0}. Their superposition allows us to define equivalent time-reversal-symmetric ground states as

$$\Phi_{j_0\pm} = \frac{1}{\sqrt{2}}\big(\Psi_{j_0} \pm \Psi_{-j_0}\big). \tag{21}$$

These two ground states are not rotationally symmetric and characterized by $\langle J_z \rangle = 0$ and $\Delta J_z = j_0$. An analogous discussion for the case of SLM coupling can be found in Ref. [14].

So far, we have discussed symmetry properties of the noninteracting Hamiltonian. Most of them are expected to also be valid in the presence of collisional interactions manifested by the nonlinear term in the Hamiltonian (5). However, one crucial difference of the interacting system is a breakdown of the superposition principle for wave functions. This superposition principle is required for R-symmetric states $\Psi_{\pm j_0}$ and T-symmetric states $\Phi_{j_0\pm}$ to have the same energy. In the interacting system, their energies will be different. Therefore, if the ground state is characterized by $j_0 \neq 0$, then either rotational or time-reversal symmetry will be spontaneously broken. These symmetry breakings lead to possible existence of two different quantum phases: a stripe phase with broken R symmetry and a polarized phase with broken T symmetry [13,23]. If the ground state is characterized by $j_0 = 0$, then both symmetries can be preserved even in the presence of interactions. Such a ground state of the interacting systems is commonly termed as a zero-momentum phase. These and other possible types of ground states of the interacting system will be discussed in more detail in the next section.

C. Numerical procedure

Symmetries of the single-particle Hamiltonian provide a lot of insight into the properties of the ground state. Nevertheless, solutions of the full GPE (3) can never be obtained analytically. For numerical computations of the ground-state solution, we adopt a well-known imaginary-time evolution method [29,30]. Due to a complex energy landscape of a SOAM-coupled system, finding a true ground state becomes a numerically challenging task. To distinguish the ground state from low-lying metastable excited states, we repeat the procedure of imaginary-time evolution using different initial trial states. We construct trial states with different populations and OAM projections between $-2l$ an $2l$ in each component, as well as states with random distributions. The ground state is then determined as the final state with the lowest energy after the converged numerical procedure.

III. RESULTS AND DISCUSSIONS

For the rest of the paper, we focus on a more realistic system of weakly interacting atoms described by the full GPE (3). We consider a total number of $N = 5 \times 10^3$ particles confined in a disk-shaped harmonic trap with trapping frequencies $\omega_\rho = 1.5 \times 2\pi$ Hz and $\omega_z = 24 \times 2\pi$ Hz. For this choice of frequencies, $\omega_z \gg \omega_\rho$, the use of two-dimensional approximation is justified. The nonlinear interaction parameters are chosen as

$$g_{\uparrow\uparrow} = g_{\downarrow\downarrow} = g, \quad g_{\uparrow\downarrow} = 0.9g,$$

where $g = a\sqrt{8\pi\hbar^2\omega_z/M}$ is related to the s-wave scattering length a and the atom mass M of ^{87}Rb. This choice of nonlinear interaction parameter is reasonably close to the realistic parameters of ^{87}Rb condensate but at the same time allows us to observe many possible types of the ground state [24].

The Raman coupling (7) is characterized by the angular momentum $l = 1$ and the beam waist $w = 176\,\mu$m, which is considerably larger than the estimated Thomas-Fermi radius of the condensate $R_{\mathrm{TF}} \approx 26\,\mu$m.

Our results below are presented in dimensionless units, by adopting the oscillator energy $\epsilon_{\mathrm{ho}} = \hbar\omega_\rho$ and length $a_{\mathrm{ho}} = \sqrt{\hbar/M\omega_\rho}$ of the harmonic trap as the energy and length scales, respectively.

A. Phase diagram

We aim here to define and characterize possible types of ground states in the system. Due to a large number of parameters in the Hamiltonian, it is unfeasible to explore the entire parameter space. We therefore concentrate on a single, but most relevant control parameter, the Raman coupling strength Ω. Fig. 2 shows five examples of ground-state wave functions calculated for different values of Ω. One may see qualitative changes in the ground state depending on the coupling strength. When the coupling is weak, we can observe a deformation of the cloud from the rotationally-symmetric shape defined by the trapping potential [see Fig. 2(I)]. Stronger coupling leads to the formation of quantum vortices in the condensate, which can be identified by hollow regions in the amplitude and singularities in the phase of the wave function. By calculating the ground-state solutions in a wide range of $\Omega > 0$ we are able to identify four different spatial arrangements of vortices in the condensate [see Figs. 2(II)–2(V)].

The different types of ground-state wave functions displayed in Fig. 2 can be unambiguously related to the symmetries of single-particle Hamiltonian. To this end, we show in Fig. 3 the previously introduced symmetry indicators $\langle \hat{J}_z \rangle$, ΔJ_z, and $\langle \hat{\sigma}_z \rangle$ depending on the coupling strength Ω. We identify in total four critical values $\Omega_{c1}, ..., \Omega_{c4}$, at which both the behavior of these symmetry indicators and the spatial distribution of the wave function sharply change. These changes represent quantum phase transitions and, therefore, Fig. 3 can be seen as a phase diagram showing five phases (I–V) of the system, whose corresponding wave functions are already shown in Fig. 2.

The phase transitions identified in Fig. 3 can be classified by their orders. Adopting the Ehrenfest classification, the order of a transition is the order of the lowest derivative of energy which shows a discontinuity [31]. The first-order and second-order (continuous) phase transitions significantly differ in a way how the ground state changes with the variation of a control parameter. For the first-order transition, the ground state switches from the stationary state of one phase to that of the other phase due to an energy crossing between two states. In contrast, the continuous phase transition is characterized by the smooth transformation of the ground state. For this case, the ground-state wave functions of two phases are in-
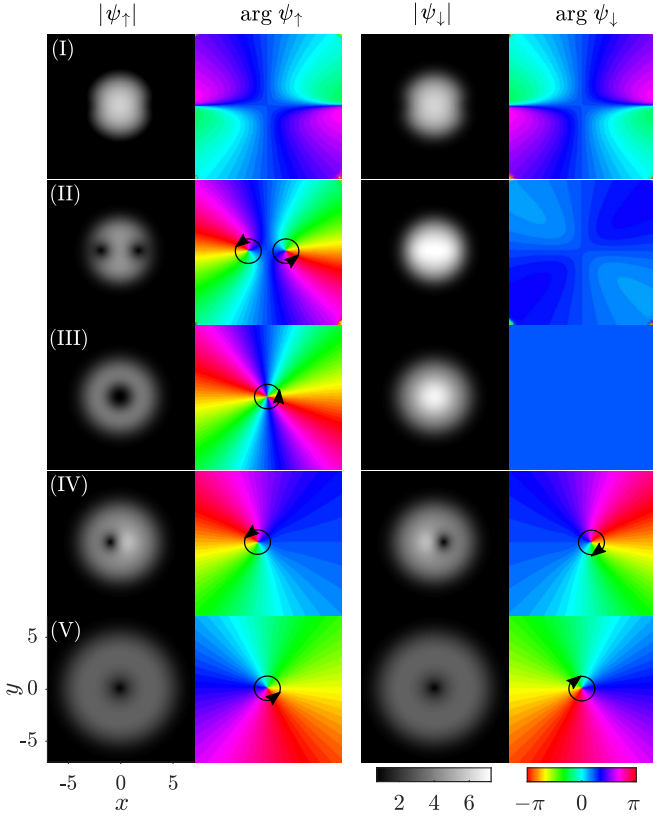
FIG. 2. Amplitudes and phases of the ground-state wave functions for up (two left columns) and down (two right columns) components at Raman coupling strengths $\Omega = 36$ (I), $\Omega = 45$ (II), $\Omega = 120$ (III), $\Omega = 150$ (IV), and $\Omega = 220$ (V). Vortices in each component are marked with circles on the phase plots. Arrows indicate directions of the phase winding. The length unit is set by $a_{\mathrm{ho}} = \sqrt{\hbar/M\omega_\rho}$.
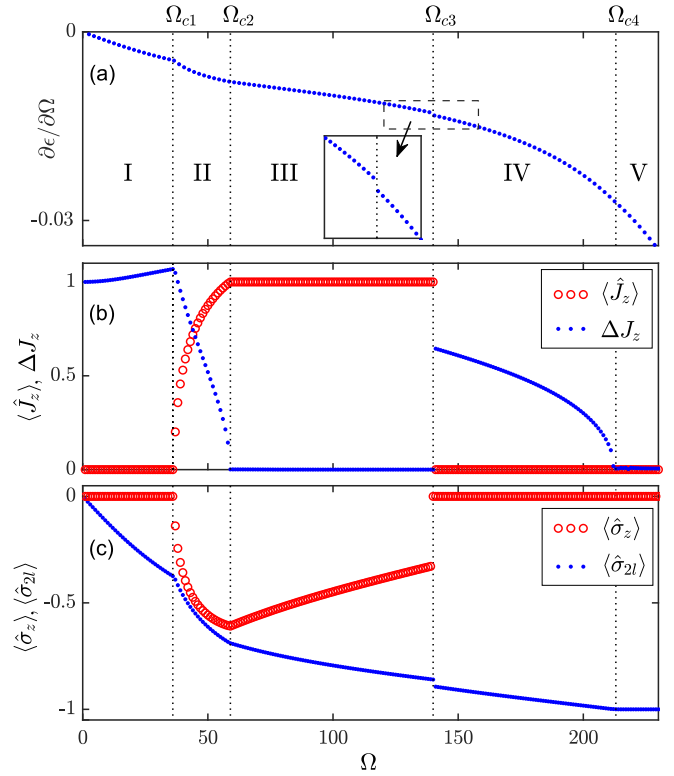

FIG. 3. Phase diagram with respect to the coupling strength Ω. Panel (a) shows the derivative of ground-state energy $\partial\epsilon/\partial\Omega$. Panel (b) shows the expectation of total angular momentum $\langle \hat{J}_z \rangle$ and its standard deviation ΔJ_z. Panel (c) shows expectation values of the spin operators $\langle \hat{\sigma}_z \rangle$ and $\langle \hat{\sigma}_{2l} \rangle$. We show here only the non-negative branch of $\langle \hat{J}_z \rangle$ and $\langle \hat{\sigma}_z \rangle$, which corresponds to one of the two degenerate ground states. Phase transitions are detected at critical Ω values $\Omega_{c1} = 36$, $\Omega_{c2} = 59$, $\Omega_{c3} = 140$, and $\Omega_{c4} = 213$.

distinguishable at the transition point. In the present paper, to determine the order of transitions, we calculate the derivative of energy with respect to the coupling strength, $\partial\epsilon/\partial\Omega$. As seen in Fig. 3(a), this quantity shows that only the transition between phases III and IV is of first order, while all other phase transitions are continuous. This observation is quite surprising, as previous works have shown that transitions in

SOAM coupled BECs are mostly of first order [21,23,24,27]. Below we will argue that this behavior is explained by the existence of phases II and IV, which possess neither of the symmetries of the Hamiltonian (4) and exhibit a nontrivial vortex structure. In particular, their wave functions contain the so-called vortex molecule, i.e., two vortices located at a distance from each other. To better understand the role of

TABLE I. Properties of the ground state in phases I–V. The upper part shows the preserved symmetries and values of three symmetry indicators. T and R denote the time-reversal and rotational symmetries, respectively. The lower part shows features of the wave function. In the last row, the total phase winding numbers of up and down components are shown in brackets.

	I Stripe phase	II Two-vortex molecule phase	III Polarized phase	IV Vortex-antivortex molecule phase	V Zero-momentum phase
Symmetry	T	–	R	–	T, R
$\langle \hat{\sigma}_z \rangle$	0	$\neq 0$	$\neq 0$	0	0
ΔJ_z	$\gtrsim 1$	$\neq 0$	0	$\neq 0$	0
$\langle \hat{J}_z \rangle$	0	noninteger	1 or -1	0	0
Degeneracy	–	twofold	twofold	–	–
Corresponding single-particle states	Φ_{1-} [see Eq. (21)]	–	Ψ_1 or Ψ_{-1} [see Eq. (15)]	–	Ψ_0 [see Eq. (15)]
Angular density stripes	+	+	–	+	–
Phase winding number	(0,0)	(+2, 0) or (0, −2)	(+2, 0) or (0, −2)	(+1, −1)	(+1, −1)

such molecules in the observed continuous transitions, we first need to discuss the properties of individual phases: I, III, and V in Sec. III B and II and IV in Sec. III C. In this discussion of various phases, special attention will be paid to the vortex structure of the wave function and its relation to the symmetry indicators. Moreover, for the sake of bookkeeping, we summarize the properties of all five phases in Table I.

B. Symmetric phases

We refer to phases I, III, and V as the symmetric phases, since each of them possesses either one or both of the symmetries of the system. These symmetries can be clearly identified from the symmetry indicators in Fig. 3. Specifically, vanishing spin polarization $\langle \hat{\sigma}_z \rangle$ in phases I and V implies the time-reversal symmetry of the ground state, while rotational symmetry can be identified in phases III and V by $\Delta J_z = 0$.

Based on the symmetry properties, it is straightforward to show that phases I, III, and V are the well-known stripe, polarized, and zero-momentum phases that have been thoroughly studied in systems with SOAM or SLM coupling [13,14,21,23]. Moreover, a correspondence can be established between each of these phases and the single-particle state with the same symmetry, as seen in Table I. For phases III and V, their wave functions resemble Eq. (15). However, for the stripe phase, Φ_{1-} defined by Eq. (21) is only a rough approximation of the many-body ground state, as suggested by $\Delta J_z \gtrsim 1$.

Before preceding to the discussion of other phases, we would like to comment on the completeness of the phase diagram. It leads us to the question whether any phases can exist beyond phase V. To answer this question, we consider the strong-coupling limit ($\Omega \rightarrow \infty$) of the system, in which the total Hamiltonian $\hat{H}$ is dominated by the Raman coupling term, $\hat{H} \approx \tilde{\Omega}(\rho)\hat{\sigma}_{2l}$. Consequently, the ground state in this regime is an eigenstate of the unitary operator $\hat{\sigma}_{2l}$ corresponding to its lowest eigenvalue -1. As seen from Fig. 3, this condition is already fulfilled in phase V, for which $\langle \hat{\sigma}_{2l} \rangle = -1$. We conclude, therefore, that phase V represents the strong-coupling limit of the system, and no other phases are expected for $\Omega > \Omega_{c4}$.

C. Vortex-molecule phases

The phase diagram in Fig. 3 shows that the three symmetric phases are separated by phases II and IV. These two intermediate phases have no counterparts in the single-particle spectrum and also do not exist in systems with SLM coupling. In this section, we will characterize these two phases and reveal the role of vortex molecule in continuous phase transitions.

1. Two-vortex-molecule phase

Phase II is observed in a relatively narrow region between the T-symmetric stripe phase and R-symmetric polarized phase. The ground-state wave function of phase II is, however, neither T nor R symmetric, as suggested by nonzero values of $\langle \hat{\sigma}_z \rangle$ and ΔJ_z. Therefore, two continuous phase transitions I–II and II–III are associated with broken time-reversal and rotational symmetry, respectively. Following a common practice for describing such transitions, we define the so-called order
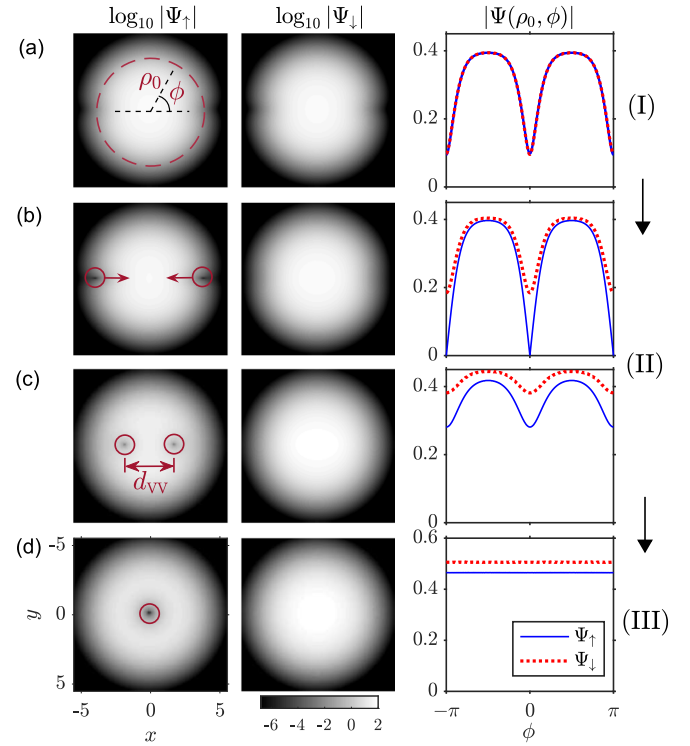

FIG. 4. Amplitudes of two wave-function components (two left columns) and corresponding azimuthal distributions (rightmost column) at the distance ρ_0 from the center (marked with a dashed circle). Four rows correspond to different values of the coupling strength: $\Omega = 36$ (a), $\Omega = 37$ (b), $\Omega = 45$ (c), $\Omega = 61$ (d). Row (a) corresponds to phase I, (b) and (c) to phase II, (d) to phase III. Vorex cores are marked with circles. The value of ρ_0 is chosen to pass through the vortex cores in the row (b). Characteristic size of two-vortex molecule is labeled as d_{VV}. The logarithmic scale is applied in two left columns for a better visibility. The length unit is set by $a_{\text{ho}} = \sqrt{\hbar/M\omega_\rho}$.

parameter, which is zero in the symmetric phase and nonzero in the symmetry-broken phase. In our paper, the symmetry indicators can be used as such order parameters. For instance, ΔJ_z, which continuously changes from nonzero in phase II to zero in phase III, is an order parameter for transition II–III. Similarly, transition I–II is characterized by $\langle \hat{\sigma}_z \rangle$ or $\langle \hat{J}_z \rangle$.

In addition to the symmetry indicators, the continuous phase transitions I $\rightarrow$ II $\rightarrow$ III can be identified by the transformation of the ground-state wave functions. For demonstration, we show in Fig. 4 the wave-function amplitudes $|\psi_\uparrow|$ and $|\psi_\downarrow|$ calculated at different Ω across the two transitions. Moreover, we include in the figure the angular dependencies of these amplitudes for an arbitrarily chosen radial position ρ_0. To describe the transitions, we start with Fig. 4(a), which displays the wave function of phase I. As expected for this T-symmetric stripe phase, $|\psi_\uparrow| = |\psi_\downarrow|$ and both components exhibit azimuthal density modulations, usually referred to as stripes. The transition I–II is marked by the formation of vortices inside these stripes in one component and simultaneous healing of the stripes of the other, as seen in Fig. 4(b). This behavior leads to the fact that $|\psi_\uparrow| \neq |\psi_\downarrow|$, which shows a breaking of T symmetry. As Ω increases further, the two vortices approach each other and finally merge
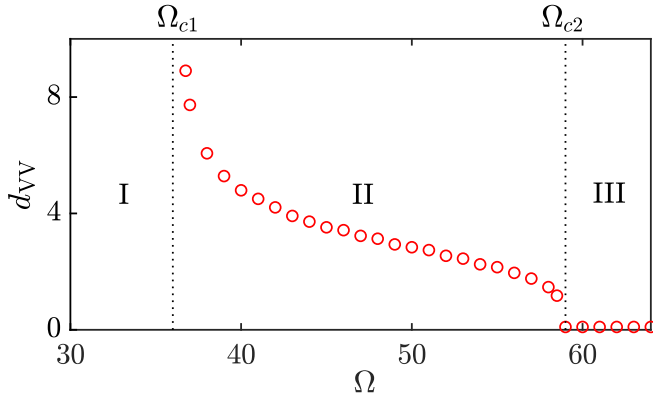
FIG. 5. Vortex molecule size d_{VV}, in units of harmonic length $a_{ho} = \sqrt{\hbar/M\omega_\rho}$, as a function of coupling strength Ω.
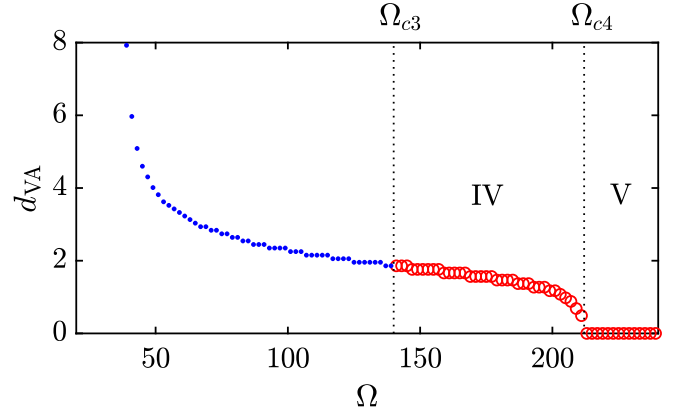

FIG. 6. Vortex-antivortex molecule size d_{VA}, in units of harmonic length $a_{ho} = \sqrt{\hbar/M\omega_\rho}$, as a function of Raman coupling strength Ω. Blue dots represent the (excited) stationary vortex-antivortex-molecule state in the region $\Omega < \Omega_{c3}$.

when the system experiences transition II–III. At the same time, the azimuthal density modulations in both components disappear and R symmetry is recovered, as expected for phase III.

One may notice that in Figs. 2 and 4, vortex molecules and density stripes are shown always oriented along the x axis. In reality, this direction is randomly chosen by the system as a result of rotational symmetry breaking. Due to invariance of the Hamiltonian under rotations (13), all orientations are equivalent and correspond to the same energy of the ground state. We show these states always oriented along the x direction only for convenience of the presentation and analysis.

To gain more insight into the role of vortices in continuous phase transitions, we show in Fig. 5 the characteristic size of the vortex molecule, d_{VV}, as a function of coupling strength Ω. Defined as the distance between two vortices, d_{VV} diverges at Ω_{c1}, monotonically decreases throughout phase II and becomes zero in phase III. We therefore argue that d_{VV} can serve as an alternative order parameter for the phase transition II–III besides the symmetry indicator ΔJ_z. In contrast to the latter, d_{VV} can be more accessible for experimental measurements.

2. Vortex-antivortex-molecule phase

Apart from the two-vortex molecule in phase II, a different vortex configuration can be detected in the ground state of phase IV. In the latter case, each condensate component contains a single vortex. These vortices possess opposite phase windings and are displaced from each other, thus forming a vortex-antivortex molecule [see Fig. 2(IV)]. The size of this molecule, d_{VA}, is displayed as a function of the coupling strength Ω in Fig. 6. Similarly to transition II–III, we see the collapse of vortex-antivortex molecule, $d_{VA} = 0$, at the formation of R-symmetric phase V. However, the behavior of d_{VA} at the other phase boundary Ω_{c3} drastically differs from the divergence of d_{VV} at $\Omega = \Omega_{c1}$ (see Fig. 5). This difference appears because transition III–IV is a first-order transition characterized by a sudden switch of the ground state between stationary states of phases III and IV. Therefore, while it is possible to trace the value of d_{VA} to $\Omega < \Omega_{c3}$, it does not describe the ground state of the system any more.

Similar to Sec. III C, the characteristic size of the vortex-antivortex molecule, d_{VA}, can be used as an order parameter

for transition IV–V. Likewise, an alternative choice can be the symmetry indicator ΔJ_z. However, in contrast to phase II, $\langle \hat{\sigma}_z \rangle$ fails to indicate the broken T symmetry in phase IV, and thus cannot serve as an order parameter. The possibility of such behavior was already mentioned in Sec. II B.

IV. SUMMARY AND OUTLOOK

In conclusion, we have provided a systematic description of the quantum phases and phase transitions in a two-component BEC with SOAM coupling. By analyzing the ground-state wave function for different values of the Raman coupling strength, we identified in total five quantum phases. Three of them possess either one or both of the time-reversal and rotational symmetries and represent the stripe, polarized, and zero-momentum phases that are well-known in systems with SLM coupling. In contrast, the other two phases have no counterparts and possess neither of the above symmetries. Moreover, complex vortex-molecule structures were observed in the wave functions of these two symmetry-broken phases. We argue that the formation and collapse of vortex molecules play an important role in the phase transitions of the system. In particular, the existence of these molecules can explain the presence of continuous phase transitions in SOAM-coupled condensates. Since these transitions were not the focus of previous studies, we carried out detailed calculations for investigating their properties. Our results showed that the symmetry indicators, as well as the characteristic size of the vortex molecules, can serve as effective order parameters characterizing these continuous phase transitions.

The experimental investigation of the predicted vortex-molecule phases is feasible with currently existing techniques. For example, the finite spin polarization, which is an indication of broken time-reversal symmetry, exhibits itself in dipole oscillations of the condensate [32]. Moreover, the vortex structure can be detected by interferometric measurements [27,33] or potentially with the Bragg-scattering technique, which has been already applied for probing the stripe phase under SLM coupling [17,34].

The present study is restricted to the Raman coupling generated by LG beams with a phase winding $l = 1$. However, the developed theory can be readily extended to higher values of l. Following our analysis, no additional symmetries appear in these cases, but more complicated multivortex molecules may exist in the condensate (see, e.g., Ref. [23]). A systematic investigation of such multivortex molecules and associated phase transitions will be presented in future publications.

[1] M. H. Anderson, J. R. Ensher, M. R. Matthews, C. E. Wieman, and E. A. Cornell, Observation of Bose-Einstein condensation in a dilute atomic vapor, Science **269**, 198 (1995).

[2] K. B. Davis, M. O. Mewes, M. R. Andrews, N. J. van Druten, D. S. Durfee, D. M. Kurn, and W. Ketterle, Bose-Einstein Condensation in a Gas of Sodium Atoms, Phys. Rev. Lett. **75**, 3969 (1995).

[3] D. M. Stamper-Kurn, M. R. Andrews, A. P. Chikkatur, S. Inouye, H.-J. Miesner, J. Stenger, and W. Ketterle, Optical Confinement of a Bose-Einstein Condensate, Phys. Rev. Lett. **80**, 2027 (1998).

[4] Y. Kawaguchi and M. Ueda, Spinor Bose–Einstein condensates, Phys. Rep. **520**, 253 (2012).

[5] Y.-J. Lin, K. Jiménez-García, and I. B. Spielman, Spin-orbit-coupled Bose-Einstein condensates, Nature **471**, 83 (2011).

[6] P. Wang, Z.-Q. Yu, Z. Fu, J. Miao, L. Huang, S. Chai, H. Zhai, and J. Zhang, Spin-Orbit Coupled Degenerate Fermi Gases, Phys. Rev. Lett. **109**, 095301 (2012).

[7] J. Dalibard, F. Gerbier, G. Juzeliūnas, and P. Öhberg, Colloquium: Artificial gauge potentials for neutral atoms, Rev. Mod. Phys. **83**, 1523 (2011).

[8] H. Zhai, Degenerate quantum gases with spin-orbit coupling: A review, Rep. Prog. Phys. **78**, 026001 (2015).

[9] N. Goldman, G. Juzeliūnas, P. Öhberg, and I. B. Spielman, Light-induced gauge fields for ultracold atoms, Rep. Prog. Phys. **77**, 126401 (2014).

[10] S. Zhang and G.-B. Jo, Recent advances in spin-orbit coupled quantum gases, J. Phys. Chem. Solids **128**, 75 (2019).

[11] T. Oshima and Y. Kawaguchi, Spin Hall effect in a spinor dipolar Bose-Einstein condensate, Phys. Rev. A **93**, 053605 (2016).

[12] M. C. Beeler, R. A. Williams, K. Jimenez-Garcia, L. J. LeBlanc, A. R. Perry, and I. B. Spielman, The spin Hall effect in a quantum gas, Nature **498**, 201 (2013).

[13] Y. Li, L. P. Pitaevskii, and S. Stringari, Quantum Tricriticality and Phase Transitions in Spin-Orbit Coupled Bose-Einstein Condensates, Phys. Rev. Lett. **108**, 225301 (2012).

[14] C. Wang, C. Gao, C.-M. Jian, and H. Zhai, Spin-Orbit Coupled Spinor Bose-Einstein Condensates, Phys. Rev. Lett. **105**, 160403 (2010).

[15] G. I. Martone, Y. Li, L. P. Pitaevskii, and S. Stringari, Anisotropic dynamics of a spin-orbit-coupled Bose-Einstein condensate, Phys. Rev. A **86**, 063621 (2012).

[16] Y. Li, G. I. Martone, L. P. Pitaevskii, and S. Stringari, Superstripes and the Excitation Spectrum of a Spin-Orbit-Coupled Bose-Einstein Condensate, Phys. Rev. Lett. **110**, 235302 (2013).

[17] J.-R. Li, J. Lee, W. Huang, S. Burchesky, B. Shteynas, F. Ç. Top, A. O. Jamison, and W. Ketterle, A stripe phase with supersolid properties in spin-orbit-coupled Bose-Einstein condensates, Nature **543**, 91 (2017).

[18] M. DeMarco and H. Pu, Angular spin-orbit coupling in cold atoms, Phys. Rev. A **91**, 033630 (2015).

[19] L. Chen, H. Pu, and Y. Zhang, Spin-orbit angular momentum coupling in a spin-1 Bose-Einstein condensate, Phys. Rev. A **93**, 013629 (2016).

[20] I. Vasić and A. Balaž, Excitation spectra of a Bose-Einstein condensate with an angular spin-orbit coupling, Phys. Rev. A **94**, 033627 (2016).

[21] K. Sun, C. Qu, and C. Zhang, Spin–orbital-angular-momentum coupling in Bose-Einstein condensates, Phys. Rev. A **91**, 063627 (2015).

[22] Yu.-X. Hu, C. Miniatura, and B. Grémaud, Half-skyrmion and vortex-antivortex pairs in spinor condensates, Phys. Rev. A **92**, 033615 (2015).

[23] C. Qu, K. Sun, and C. Zhang, Quantum phases of Bose-Einstein condensates with synthetic spin–orbital-angular-momentum coupling, Phys. Rev. A **91**, 053630 (2015).

[24] X.-L. Chen, S.-G. Peng, P. Zou, X.-J. Liu, and H. Hu, Angular stripe phase in spin-orbital-angular-momentum coupled Bose condensates, Phys. Rev. Research **2**, 033152 (2020).

[25] K.-J. Chen, F. Wu, J. Hu, and L. He, Ground-state phase diagram and excitation spectrum of a Bose-Einstein condensate with spin-orbital-angular-momentum coupling, Phys. Rev. A **102**, 013316 (2020).

[26] H.-R. Chen, K.-Y. Lin, P.-K. Chen, N.-C. Chiu, J.-B. Wang, C.-A. Chen, P.-P. Huang, S.-K. Yip, Y. Kawaguchi, and Y.-J. Lin, Spin–Orbital-Angular-Momentum Coupled Bose-Einstein Condensates, Phys. Rev. Lett. **121**, 113204 (2018).

[27] D. Zhang, T. Gao, P. Zou, L. Kong, R. Li, X. Shen, X.-L. Chen, S.-G. Peng, M. Zhan, H. Pu, and K. Jiang, Ground-State Phase Diagram of a Spin-Orbital-Angular-Momentum Coupled Bose-Einstein Condensate, Phys. Rev. Lett. **122**, 110402 (2019).

[28] M. D. Lee, S. A. Morgan, M. J. Davis, and K. Burnett, Energy-dependent scattering and the Gross-Pitaevskii equation in two-dimensional Bose-Einstein condensates, Phys. Rev. A **65**, 043617 (2002).

[29] L. Lehtovaara, J. Toivanen, and J. Eloranta, Solution of time-independent Schrödinger equation by the imaginary time propagation method, J. Comput. Phys. **221**, 148 (2007).

[30] W. Bao and Q. Du, Computing the ground state solution of Bose–Einstein condensates by a normalized gradient flow, SIAM J. Sci. Comput. **25**, 1674 (2004).

[31] L. D. Landau and E. M. Lifshitz, *Statistical Physics, Course of Theoretical Physics*, Vol. 5 (Pergamon Press Ltd., London, 1958).

[32] J.-Y. Zhang, S.-C. Ji, Z. Chen, L. Zhang, Z.-D. Du, B. Yan, G.-S. Pan, B. Zhao, Y.-J. Deng, H. Zhai, S. Chen, and J.-W. Pan, Collective Dipole Oscillations of a Spin-Orbit Coupled Bose-Einstein Condensate, Phys. Rev. Lett. **109**, 115301 (2012).

[33] K. C. Wright, L. S. Leslie, A. Hansen, and N. P. Bigelow, Sculpting the Vortex State of a Spinor BEC, Phys. Rev. Lett. **102**, 030405 (2009).

[34] A. Putra, F. Salces-Cárcoba, Y. Yue, S. Sugawa, and I. B. Spielman, Spatial Coherence of Spin-Orbit-Coupled Bose Gases, Phys. Rev. Lett. **124**, 053605 (2020).